Poly-disperse simulation of flash evaporation of water inside a large vertical pipe using class method of population balance

Liao, Y.; Lucas, D.;

Originally published:

May 2019

International Journal of Heat and Fluid Flow 77(2019), 299-313

DOI: https://doi.org/10.1016/j.ijheatfluidflow.2019.05.005

Perma-Link to Publication Repository of HZDR:

https://www.hzdr.de/publications/Publ-28144

Poly-disperse simulation of flash evaporation of water inside a large vertical pipe using class method of population balance

Yixiang Liao*, Dirk Lucas

Helmholtz-Zentrum Dresden - Rossendorf, Institute of Fluid Dynamics
Bautzner Landstraße 400, 01328 Dresden, Germany

Abstract

Flash evaporation of superheated liquid to vapour by depressurization is frequently encountered in the nature and technology, but computational fluid dynamics modelling and simulation of such scenarios is still at the embryo stage. Attempts having been made before are all based on the assumption of mono-disperse bubbles by prescribing either the size or number density, which deviates largely from the physical picture. In the present work the poly-disperse multiple-size-group approach is used for the first time to simulate the water evaporation process under pressure release transients. Complex bubble dynamics and non-equilibrium processes such as bubble nucleation, growth, coalescence and breakup as well as interfacial heat transfer are accounted for. The comparison with experimental data demonstrates that the model is effective in capturing the temporal course of vapour bubbles' generation and growth as well as their spatial distribution. The agreement between measured and simulated cross-section averaged flow parameters such as void fraction, liquid temperature and bubble size distribution is satisfying.

Keywords: bubble coalescence; bubble nucleation; flash evaporation; interfacial heat transfer; poly-disperse

1. Introduction

Pressure release through safety or blow-off valves is of great interest in many situations which apply to the safety strategy of chemical, process and nuclear plants. One well-known phase change phenomenon encountered during a pressure release process is "flash boiling (or evaporation)", namely, sudden evaporation of initially sub-cooled liquid without infusion of heat. Here the term "flash" is used to distinguish it from the traditional boiling phenomena occurring at heated walls. Similar scenes can take place as hydrostatic pressure decreases in a gravity-driven pipe flow, dynamic pressure changes in nozzles, or sub-cooled liquid discharged from a pressurized container through cracks or slits. The formation and growth of vapour bubbles in the liquid affects the thermal-hydraulic behaviour of the flow significantly, but reliable numerical analysis of such effects represents still huge challenges partly due to the lack of high-resolved experimental data. The flash evaporation process is controlled by thermal and mechanical non-equilibrium across the bubble surface. In the boundary layer around the bubble surface velocity and temperature fields are evolving rapidly in both time and space, which made these measurements inaccessible until recently [1]. Further, knowledge about the physics of bubble dynamics such as nucleation, departure, growth and shrinkage as well as the interfacial transfer processes is far from sufficient [2], which makes it difficult to incorporate the effect of these sub phenomena on the evolution of macroscopic flow

* Corresponding author: Tel. +49 351 2602389; Email: y.liao@hzdr.de

parameters in the numerical simulation. So far one-dimensional approaches or system codes are routinely applied to deal with these situations, e.g. flash atomization of fuel liquid in nozzles [3, 4] or flashing-induced instability in a natural circulation [5, 6], or critical flow problems [7, 8]. However, the flashing two-phase mixture has a strongly three-dimensional nature, which is accompanied with large heterogeneous gaseous structure and high gas volume fraction. All of these features together with rapid bubble dynamic processes at the micro-scale require a more sophisticated prediction tool with high time and space resolution such as CFD (Computational Fluid Dynamics) technology.

2. State of the art of CFD simulation of flashing flow

Since the beginning of this century promising CFD research on flashing flows has been published such as [9-16]. Nevertheless, all these investigations rely on a mono-disperse treatment of the vapour phase, which deviates largely from the physical picture of flow with rapid phase change. A review on the state of the art of CFD simulation of flash evaporation is given by Liao et al. [17]. Laurien and his co-workers studied water evaporation and re-condensation phenomena caused by steady-state pressure variation inside a 3D complex pipeline [9-12]. Frank [13] simulated the well-known Edwards pipe blow-down test [18] using a 1D simplified mesh in ANSYS CFX. Both of them prescribed a constant bubble size, e.g. d_g=1 *mm*, and employed a **5-Equation model** including two continuity equations, two momentum equations for liquid and vapour, respectively, and one energy equation for liquid. The vapour was assumed to remain always at the saturation condition corresponding to local pressure. The momentum interaction between phases is modelled only as a drag force while the effect of non-drag forces is ignored. However, Liao et al. [19] showed that non-drag forces have a significant effect on the spatial distribution of phases and thus local interfacial transfer rates. A 5-equation model including both drag and non-drag forces was presented in [20] and used for the simulation of flash evaporation of water inside a large vertical pipe under pressure release transient at different pressure levels (10 bar, 20 bar, 40 bar, 65 bar). The uncertainty in predictions for the onset of flashing due to the prescribed value for bubble size was discussed. Laurien [12] suggested that a model presuming bubble number density, which allows bubble size grow, is more close to the physical picture of boiling flow in comparison with the prescription of bubble size. The assumption is acceptable when the nucleation zone is sufficiently narrow and bubble coalescence and breakup is negligible. The method was adopted for the simulation of flash evaporation of water through a converging-diverging nozzle by Liao et al. [21], and flashing-induced instability in a natural-circulation loop by Liao et al. [22], respectively. A more advanced approach is to introduce an additional transport equation for the bubble number density such as in [2, 14-15] as shown below. In this way, both bubble size and number density is allowed to change spatially and temporally for example due to nucleation, but it is still a mono-disperse approach, since bubble size in each computational cell has a single value instead of a spectrum at a given point in time. Maksic and Mewes [14] simulated flashing flows in pipes and nozzles by using a **4-Equation model**, where a common velocity field is assumed for both phases. The interphase heat transfer is assumed to be dominated by conduction. However, it has been shown that in most flash expansion cases the convective contribution due to relative motion of bubbles dominates the heat transfer [23], and the neglect of interphase velocity slip may lead to significant under-prediction of the vapour generation rate [24]. Wall nucleation was considered as a unique source of bubble number density. The Jones model [8, 25] was used to determine the nucleation rate. Interphase mass, momentum and energy transfer due to nucleation was ignored. Marsh [15] simulated the nozzle flashing flow using a **6-Equation model** in the commercial CFD code Fluent, with separate mass,

momentum and enthalpy balance equations for liquid and vapour. Interphase mass and momentum as well as energy transfer resulting from both nucleation and phase change were accounted. However, the effects of non-drag forces on momentum exchange and the heat transfer between vapour and vapour-liquid interface were neglected. A modified version of Blander and Katz [26] nucleation model was employed to compute the source term for the transport equation of bubble number density. The original model was found to create large numerical instability, which is based on the classical homogeneous nucleation theory. Mimouni et al. [16] simulated the cavitating flow using a **6-Equation model** in NEPTUNE_CFD. The vapour temperature was ensured to be very close to the saturation temperature by using a special heat transfer coefficient. Besides the drag, added mass and lift force was included in the interphase momentum transfer. The contribution of nucleation to the vapour generation rate as well as momentum and energy transfer was considered by the slightly modified Jones model [8]. The original model was shown to be insufficiently general by the authors. Nevertheless, the effect of nucleation and vaporisation on the mean bubble size was ignored, namely, a constant bubble size was assumed. Janet et al. [2] studied the performance of various nucleation models in a flashing nozzle flow. It was found that predictions obtained with the Jones model [8] are more reliable than the RPI [27] and Riznic models [7] under flashing conditions. In addition, the mono-disperse approach with an additional transport equation for bubble number density was shown to have inherent limitations in reproducing the bubble dynamics and thus phase distribution properly.

The limitation and possibility of the CFD technology for the simulation of flash evaporation is discussed in detail in [28]. The necessity of poly-disperse simulation in some circumstances is confirmed. The purpose of the present work is to develop and validate a poly-disperse method for the simulation of water evaporation inside a vertical pipe under controlled pressure release conditions, where a broad size spectrum is observed experimentally [29]. Bubble coalescence in addition to nucleation is considered, and a mechanistic model is proposed for the computation of interfacial heat transfer coefficient. The reminder of the paper is organized as follows. After a short introduce to the experiment that is simulated in section 3, a detailed mathematical description of the transport equations and major closure relations is given in section 4. The simulation setup and results as well as the comparison with experimental data are presented in section 5. Suggestions for future work in section 6 conclude the paper.

3. Pressure release experiment

The test cases and data involved in this work are on the basis of the TOPFLOW pressure release experiment on a large vertical pipe test section. For details about the multi-purpose thermal-hydraulic test facility TOPFLOW the reader are referred to the work of Schaffrath et al. [30] as well as our previous work. As shown in Fig. 1(a) during the pressure release experiment, water is circulated with a velocity of about 1 m/s and flows upwards through the vertical test section. The transient pressure course is controlled by the blow-off valve located above the steam drum, where saturation conditions are always guaranteed. As a result, cavitation in the circulation pump below is avoided. At the same time, the maximum evaporation rate in the test section is limited. The inlet water temperature at the test section, which is almost equal to the saturation temperature in the steam drum, carries also the information of pressure release rate. The blow-off valve is opened to a maximum level and closed again according to a ramp shape as shown in Fig. 1(b). The opening speed of the valve is controlled by time t_1, while the maximum opening degree and its duration is represented by R and t_2. Correspondingly, the generation and disappearance of

steam is determined by the operation of the valve. Data for different t_1, t_2, R and pressure levels are available (see Fig. 1(c)). A detailed introduction to the experimental procedure and data was given by Lucas et al. [29]. The effect of the pressure level was investigated in [20] by performing mono-disperse simulations for the four cases in Test 1. The poly-disperse approach presented in this work is aimed to enhance the versatility of the numerical model by avoiding the free parameter of bubble size or bubble number density. Simulation results of an example case at 20 MPa (t_1 = 14s, t_2 = 42s, R =40%), which is highlighted with the yellow color in Fig. 1(c), are presented in Section 5 below.

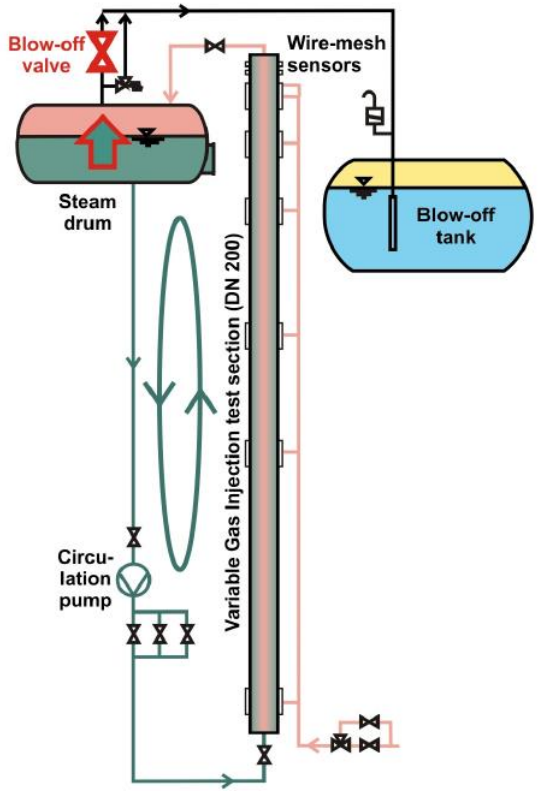

(a)

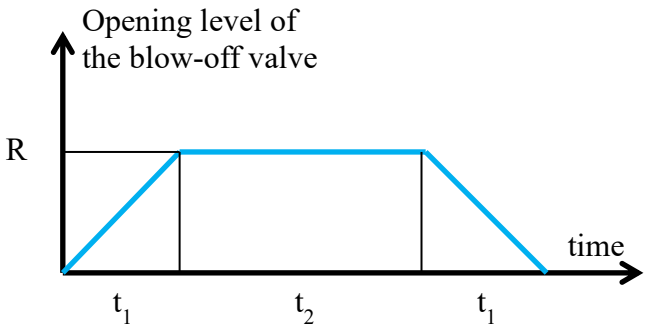

(b)

	Test 1			Test 2		
p	R	t_1	t_2	R	t_1	t_2
MPa	%	s	s	%	s	s
1	60	21	30	50	18	34
2	50	18	34	40	14	42
4	30	11	48	25	9	52
6.5	25	9	52	20	7	56

(c)

Fig. 1 General information about the experimental procedure and conditions

4. Physical setup

4.1. Fundamental transport equations

The five-equation two-fluid model with source terms for interphase exchange under adiabatic conditions is represented by Eq. (1) ~ Eq. (5) for the liquid and gas phase, respectively.

Liquid phase:

$$\frac{\partial}{\partial t}\left(\alpha_l \rho_l\right)+\nabla\cdot\left(\alpha_l \rho_l \vec{U}_l\right)=\Gamma_l \quad , \tag{1}$$

$$\frac{\partial}{\partial t}\left(\alpha_l \rho_l \vec{U}_l\right)+\nabla\cdot\left(\alpha_l \rho_l \vec{U}_l \otimes \vec{U}_l\right)=-\alpha_l \nabla p+\nabla\cdot\left[\alpha_l \mu_{eff,l}\left(\nabla \vec{U}_l+\left(\nabla \vec{U}_l\right)^T\right)\right]+\alpha_l \rho_l \vec{g}+\Gamma_l \vec{U}_l+\vec{F}_l \quad , \tag{2}$$

$$\frac{\partial}{\partial t}\left(\alpha_l\rho_l\left(H_{tot,l}-\frac{p}{\rho_l}\right)\right)+\nabla\cdot\left(\alpha_l\rho_l\vec{U}_l H_{tot,l}\right)=\nabla\cdot\left[\alpha_l\lambda\nabla T_l\right]+\Gamma_l H_{tot,l}+E_l \quad , \tag{3}$$

with $H_{tot,l}=C_{p,l}T_l+\frac{1}{2}\left|\vec{U}_l\right|^2$.

Gas phase:

$$\frac{\partial}{\partial t}\left(\alpha_g\rho_g\right)+\nabla\cdot\left(\alpha_g\rho_g\vec{U}_g\right)=\Gamma_g, \tag{4}$$

$$\frac{\partial}{\partial t}\left(\alpha_g\rho_g\vec{U}_g\right)+\nabla\cdot\left(\alpha_g\rho_g\vec{U}_g\otimes\vec{U}_g\right)=-\alpha_g\nabla p+\nabla\cdot\left[\alpha_g\mu_{eff,g}\left(\nabla\vec{U}_g+\left(\nabla\vec{U}_g\right)^T\right)\right]+\alpha_g\rho_g\vec{g} \tag{5}$$
$$+\Gamma_g\vec{U}_g+\vec{F}_g \quad .$$

The unknown terms Γ_k, F_k and E_k (k=l, g) represent the volumetric transfer rate of mass, momentum and energy across the gas-liquid interface, respectively, which have to be modelled by additional constitutive relations. The terms circled by green colour are secondary momentum and heat fluxes accompanied with the phase change. The major assumptions hidden above equations are that the steam and water is in pressure equilibrium and steam has always the saturation temperature corresponding to local absolute pressure. Physical properties and saturation conditions are interpolated from the published IAPWS-IF97 steam-water property tables.

4.2. Main closure models

To solve the transport equations given by Eq. (1) ~ Eq. (5) in a closed form, sub closure models are required to determine the exchanging terms Γ_k, F_k and E_k. The baseline model presented in our previous work such as [31-33], which prescribes a fixed set of closures for two-fluid modelling of bubbly flows, is aimed to minimize the uncertainty related to model selection. It is extended to include phase change in this work. Due to limited space, here only correlations related to phase change and bubble dynamics are introduced. Others such as interfacial forces and two-phase turbulence modelling remain the same as that in isothermal cases since so far no knowledge regarding the effect of phase change is available.

4.2.1 Interphase mass transfer

From the physical point of view, there are three sources for interphase mass transfer during the flash evaporation of superheated liquid, i.e.

$$\Gamma_g=-\Gamma_l=\Gamma_{phc}+\Gamma_{nuc}+\Gamma_{bgr}\,, \tag{6}$$

where Γ_{phc} represents thermal phase change induced by interphase heat transfer, Γ_{nuc} thermal nucleation and Γ_{bgr} mechanical expansion due to pressure non-equilibrium. Mathematically they are expressed as:

$$\Gamma_{phc}=\frac{-E_l\cdot A_i}{H_{tot,g}-H_{tot,l}}\,, \tag{7}$$

$$\Gamma_{nuc} = \rho_g \frac{\pi}{6} d_{nuc}^3 \cdot \underbrace{\left.\frac{dn_b}{dt}\right|_{\text{nuc}}}_{\text{nucleation rate}}, \tag{8}$$

$$\Gamma_{bgr} = \rho_g \frac{\pi d_b^2}{2} n_b \cdot \underbrace{\left.\frac{dd_b}{dt}\right|_{mech}}_{\text{bubble growth rate}}, \tag{9}$$

where d_{nuc} is bubble departure diameter in the nucleation process, and $(dn_b/dt)_{\text{nuc}}$ is the volumetric nucleation rate. Both of them have to be provided by additional closure models, which will be introduced later. The growth rate dd_b/dt is a function of pressure discontinuity at the interface, i.e. $(p_g\text{-}p_l)|_{\text{int}}$. Since the steam and water are assumed in pressure equilibrium and no pressure jump across the interface is considered, Γ_{bgr} is equal to zero in the current work.

Quantities A_i, n_b and d_b are interfacial area density, bubble number density and Sauter mean bubble size, respectively. They are related to the void fraction as follows:

$$A_i = 6\frac{\alpha_g}{d_b}, \tag{10a}$$

$$n_b = 6\frac{\alpha_g}{\pi d_b^{\,3}}. \tag{10b}$$

4.2.2 Interphase heat transfer

The sensible heat flux transferring from the steam-water interface to water, E_l, is given by:

$$E_l = h_l\left(T_{sat} - T_l\right), \tag{11}$$

where h_l is the overall heat transfer coefficient across the liquid boundary layer around a steam bubble. A variety of correlations are available for the estimation of h_l. They are derived either theoretically by considering single heat transfer mechanism such as conduction or convection or empirically by correlating experimental data under certain conditions. As a result, the validity of their application as well as extrapolation is often not guaranteed. For example, the widely-accepted Ranz-Marshall correlation [34] under-predicts significantly the heat transfer rate between a bubble and the surrounding liquid at high superheat and turbulence degree, since it was derived from the experiment on spherical water droplets evaporating in warm air. A literature survey and evaluation of existing models was given by Liao et al. [24]. The mechanistic model proposed by Liao et al. [35], which take into account heat conduction and convection as well as the effect of turbulence, is adopted in this work. It is formulated as follows

$$Nu = \frac{12}{\pi} Ja + \frac{2}{\sqrt{\pi}} Pe^{1/2} + \frac{2}{\sqrt{\pi}} Pe_t^{\,1/2} \frac{d_b}{l_{turb}}, \tag{12}$$

where Nu, Ja, Pe are Nusselt number, Jakob number and Péclet number, respectively. Their definitions are expressed as

$$Nu = \frac{d_b h_l}{\lambda_l}, \quad Ja = \frac{\rho_l c_{p,l}\left|T_{sat} - T_l\right|}{\rho_g L}, \quad Pe = \frac{d_b\left|\vec{U}_g - \vec{U}_l\right|}{a_l}, \quad Pe_t = \frac{l_{turb} u_{turb}}{a_l}.$$

Wherein λ_l, $c_{p,l}$, a_l are thermal conductivity, isobaric heat capacity and thermal diffusivity of the liquid phase, and L symbolizes the latent heat of evaporation. The first, second term on the right hand side of Eq. (12) respectively represents the heat conduction and the convection due to translational motion. The last term describes the turbulence enhancement. The turbulence length and velocity scale, l_{turb} and u_{turb}, are determined in accordance to the two-equation RANS model that used in this work

$$l_{turb} = C_\mu^{3/4} \frac{k^{3/2}}{\varepsilon}, \quad u_{turb} = C_\mu^{1/4} k^{1/2},$$

and k, ε are turbulence kinetic energy and dissipation rate. The constant C_μ has the value of 0.09.

4.2.3 The multiple-size-group (MUSIG) approach

The mean bubble size, d_b, a key parameter in all transfer terms, is provided by the MUSIG model. It is a class method of population balance and divides the bubble size spectrum into a number of groups. The poly-dispersity of bubble velocity can be considered by solving several momentum equations for different groups. In the present work only one momentum equation is solved for the gas phase, it is called homogeneous MUSIG, which is described schematically in Fig. 2.

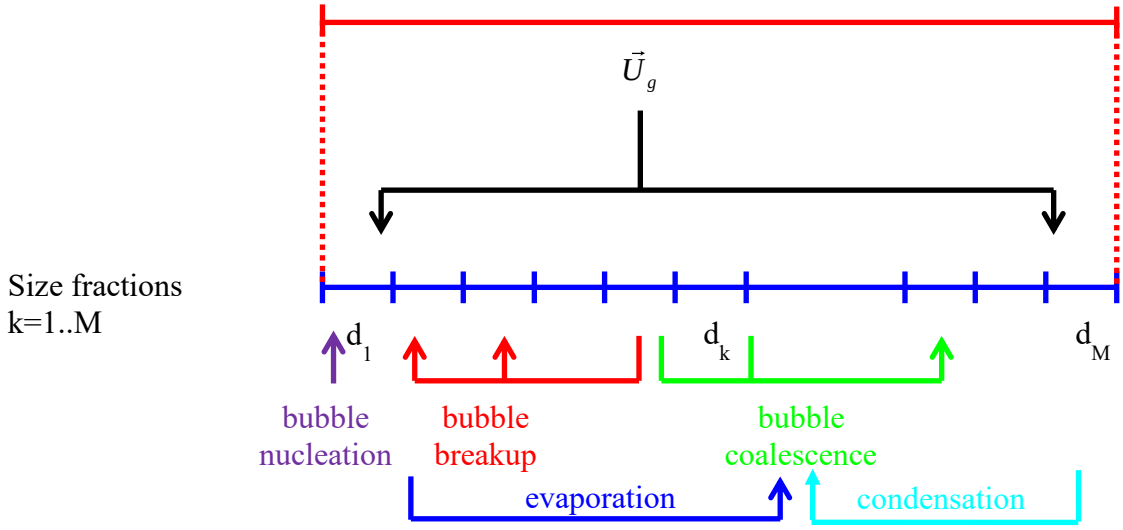

Fig. 2. Schema of homogeneous MUSIG model [36]

Additional transport equations shown in Eq. (13) are solved for the size fractions f_i, which can be transformed to the well-known population balance equation for the number density function. On the right hand side of the equations are source/sink terms due to bubble nucleation, coalescence and breakup, and phase change.

$$\frac{\partial}{\partial t}\left(\alpha_g \rho_g f_i\right) + \nabla \cdot \left(\alpha_g \rho_g f_i \vec{U}_g\right) = S_{ph,i} + S_{nuc,i} + S_{coal,i} + S_{br,i}, \tag{13}$$

where the size fraction is defined as $f_i = \alpha_i / \alpha_g$ with α_i the volume fraction of group i. As a result, the change of Sauter mean bubble size, d_b, is traced dynamically by means of its definition:

$$d_b = \frac{1}{\sum_i \frac{f_i}{d_i}}, \tag{14}$$

and d_i is the representative diameter of each group.

4.2.4 Phase change

The source/sink term, $S_{ph,i}$, due to phase change is related to interphase mass transfer rate Γ_g given in Eq. (6) as well as the discretisation of size groups [37].

$$S_{ph,i} = \frac{m_i}{m_i - m_{i-1}}\Gamma_{i-1} - \frac{m_i}{m_{i+1} - m_i}\Gamma_i \qquad \text{for evaporation } (\Gamma_i > 0), \tag{15a}$$

$$S_{ph,i} = \frac{m_i}{m_i - m_{i-1}}\Gamma_i - \frac{m_i}{m_{i+1} - m_i}\Gamma_{i+1} \qquad \text{for condensation } (\Gamma_i < 0), \tag{15b}$$

where the phase change rate of size group i, Γ_i, is related to overall bulk phase change rate, Γ_g, in the following way,

$$\Gamma_i = f_i \frac{d_b}{d_i}\Gamma_g \quad . \tag{16}$$

The symbol m_i, m_{i-1}, m_{i+1} in Eq. (15a) and Eq. (15b) represents the mass of a single bubble in the size group i, i-1 and i+1, respectively.

4.2.5 Bubble coalescence and breakup

The coalescence and breakup source terms in the population balance contain usually integrals over the bubble size, which lead to integro-differential equations and mathematical manipulations needed during the discretization [38]. For binary events they can be expressed as

$$\begin{aligned} S_{coal,i} = {} & \rho_g^2 \alpha_g^2 \frac{1}{2} \sum_{j \le i} \sum_{k \le i} C\left(m_j, m_k\right) X_{jki} f_j f_k \frac{m_i}{m_j m_k} \\ & - \rho_g^2 \alpha_g^2 \sum_j C\left(m_i, m_j\right) f_i f_j \frac{1}{m_j} \end{aligned}, \tag{17a}$$

$$\begin{aligned} S_{br,i} = {} & \rho_g \alpha_g \sum_{j \ge i} \frac{m_i}{m_j} \left(B\left(m_j, m_i\right) f_j \Delta m_i + \sum_{k \ge 1} B\left(m_j, m_k\right) f_j \Delta m_k Y_{jki} \right) \\ & - \rho_g \alpha_g \sum_{j=1}^{i} B(m_i, m_j) f_i \Delta m_j \end{aligned}. \tag{17b}$$

The fraction of mass due to coalescence between group j and k, and breakup of group j to k, which goes into the group i, is determined by the matrixes X_{jki}, Y_{jki}, respectively.

$$X_{jki}=\begin{cases}\dfrac{\left(m_j+m_k\right)-m_{i-1}}{m_i-m_{i-1}} & m_{i-1}\le m_j+m_k<m_i\\ \dfrac{m_{i+1}-\left(m_j+m_k\right)}{m_{i+1}-m_i} & m_i\le m_j+m_k<m_{i+1}\\ 0 & \text{otherwise}\end{cases},\quad Y_{jki}=\begin{cases}\dfrac{\left(m_j-m_k\right)-m_{i-1}}{m_i-m_{i-1}} & m_{i-1}\le m_j-m_k<m_i\\ \dfrac{m_{i+1}-\left(m_j-m_k\right)}{m_{i+1}-m_i} & m_i\le m_j-m_k<m_{i+1}\\ 0 & \text{otherwise}\end{cases}$$

In addition, the mirror symmetry with respect to $m_i = 0.5m_j$ of the breakage event results in the expression for the integral interval as

$$\Delta m_i=\begin{cases}m_{i+1}-m_i & m_{i+1}\le m_j/2\\ m_j/2-m_i & m_i<m_j/2<m_{i+1}\\ 0 & \text{otherwise}\end{cases}. \tag{18}$$

In Eq. (17a) and Eq. (17b) the function $C(m_j, m_k)$ represents the coalescence rate between a bubble from the group j and group k, and $B(m_j, m_k)$ the breakup rate of a bubble from the group j breaking up to a bubble from the group k, respectively. A general-applicable model has been developed in the previous work. Besides turbulence, the effect of mean velocity gradient, interfacial slip or buoyancy as well as wake-entrainment is considered in the model. Its generality has been tested for air-water and steam-water pipe flows. For more details the reader is referred to the previous work of Liao et al. [31] and Liao and Lucas [39]. Considering the overwhelming contribution of coalescence during flashing as observed in the experiment, the effect of bubble breakup is omitted in the present study.

4.2.6 Nucleation

The nucleation source is added wholly to the smallest size group, i.e., the group 1 (see Fig. 2). Two kinds of nucleation mechanisms are considered, namely, wall nucleation and bulk nucleation [2].

$$S_{nuc,1}=S_{nuc,1,W}+S_{nuc,1,B}. \tag{19}$$

Nucleation due to wall cavities is implemented through boundary source, which is transformed to a volumetric source in following way:

$$S_{nuc,1,W}=J_{het,1,W}\frac{A_{cell,W}}{V_{cell,W}}, \tag{20}$$

where $A_{cell,W}$ and $V_{cell,W}$ are the wall-side surface area and volume of the cells adjacent to the wall, respectively. The nucleation rate, $J_{het,1,W}$, is computed with aid of the Jones model [8].

$$J_{het,1,W}=\frac{\pi d_1^{\,3}}{6}\rho_g\left[0.25\times10^{-3}\left(T_l-T_{sat}\right)^3\frac{R_{nuc}^2}{R_{cr}^4}\right]\left[K^{-3}s^{-1}\right]\left(\frac{d_{nuc}}{d_1}\right)^2, \tag{21}$$

where R_{nuc}, d_{nuc} and R_{cr} are bubble departure radius, diameter and critical radius, respectively. The term $(d_{nuc}/d_1)^2$ is introduced to assure that the interfacial area density of nucleated bubbles remains constant as they are assigned to the first size group.

Heterogeneous nucleation due to impurities in the bulk flow is accounted for with the model given by Rohatgi and Reshotko [40].

$$S_{nuc,1,B} = \frac{\pi d_1^{\,3}}{6}\rho_g N_{im,B}\sqrt{\frac{2\sigma}{\pi m_W}}\exp\left(-\frac{16\pi\sigma^3\varphi}{3k_B T_l}\left(\frac{T_{sat}}{T_l - T_{sat}}\frac{\rho_g^{\,-1}-\rho_l^{\,-1}}{L}\right)^2\right)\left(\frac{d_{cr}}{d_1}\right)^2, \quad (22)$$

where d_{cr} is the critical bubble diameter, m_w the mass of a single liquid molecule and k_B is the Boltzmann constant, L latent heat. $N_{im,B}$ is the number density of impurities (nucleation sites) in the bulk and φ is the heterogeneous factor. Both $N_{im,B}$ and φ are treated as adjustable constants due to uncertainty, $N_{im,B} = 5\text{x}10^3\ m^{-3}$ and $\varphi=10^{-6}$ adopted in this work.

5. Simulation setup and results

5.1 Simulation setup

It is assumed that the flow is axis symmetrical. Instead of the whole pipe only a small wedge with an angle of 2 degrees is simulated (see Fig. 3(a)). The extension in the axial and radial direction is 8.97 m and 0.9765 m, respectively. The position for comparison between the simulation and measurement results is located at z=7.963 m. As shown in Fig. 3(b) a quasi-2D mesh is applied for the simulation. There is one layer of cells in the azimuthal direction, and symmetry boundary conditions are applied to the front and back planes.

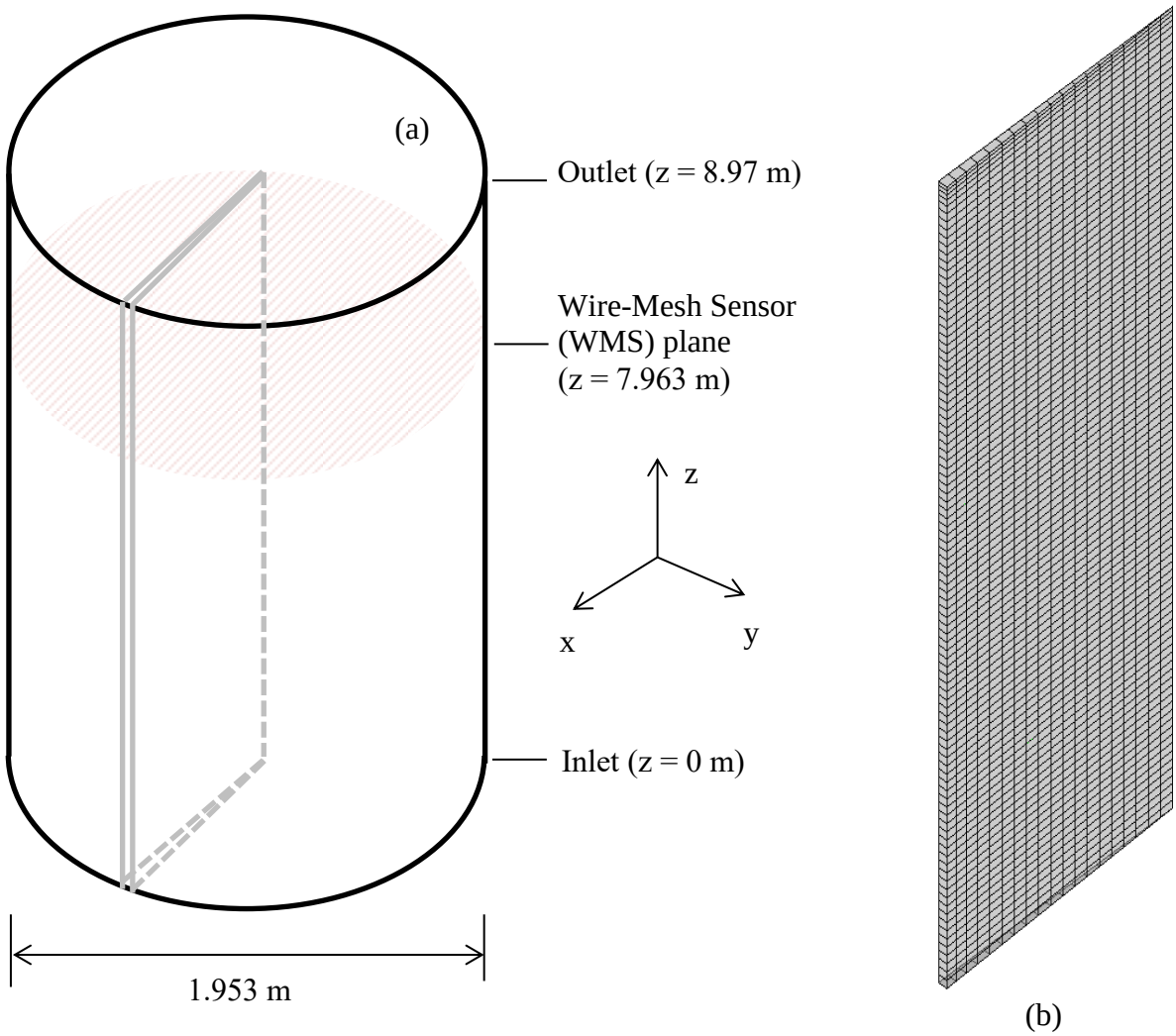

Fig. 3 Sketch of the computational domain and applied mesh

At the inlet single-phase liquid is assumed, and its mass flow rate and temperature are specified according to the experimental data. Pressure boundary condition is applied to the outlet, and the transient pressure is provided by the measurement. The wall is smooth and adiabatic. Free-slip and no-slip conditions are assigned to the gas and liquid, respectively. The temporal course of mass flow rate, inlet liquid temperature and outlet pressure are depicted in Fig. 4(a) ~ Fig. 4(c). Further, the interphase mass transfer due to wall nucleation is added to the gas and liquid continuity equations by means of wall boundary sources.

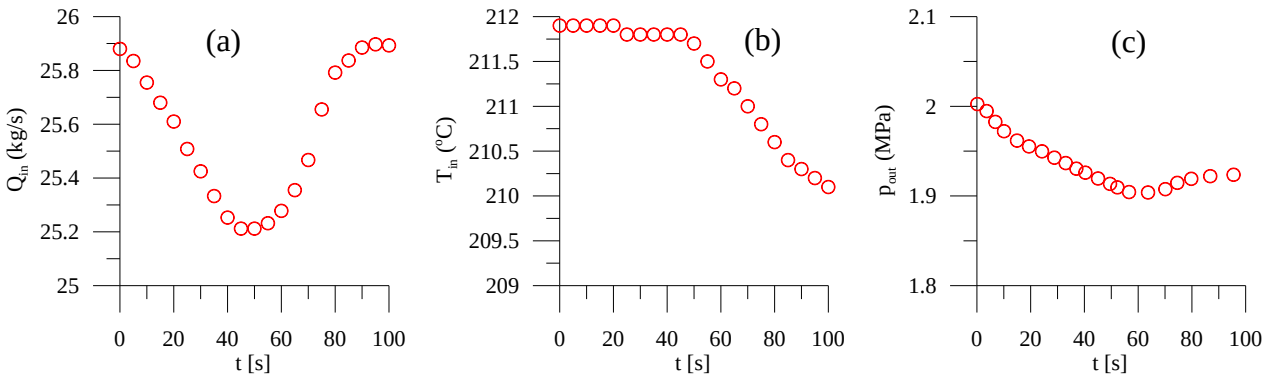

Fig. 4 Boundary conditions for simulation provided by experimental data (a) inlet mass flow rate (b) inlet liquid temperature (c) outlet absolute pressure

Initially, subcooled water flows upwards through the domain. The void fraction is equal to a small value given by the code, e.g. $\alpha_{g,ini}=10^{-15}$. The size range of bubbles is prescribed to vary from 0 mm to 63mm, and is divided into 21 size groups. Their representative diameters and initial conservative size fractions are given as follows:

Tab. 1 Discretization of bubble size and initial distribution

Group no.	**d_i [mm]**	**f_i [-]**
1	1.5	1
2	4.5	0
3	7.5	0
4	10.5	0
5	13.5	0
6	16.5	0
7	19.5	0
8	22.5	0
9	25.5	0
10	28.5	0
11	31.5	0
12	34.5	0

13	37.5	0
14	40.5	0
15	43.5	0
16	46.5	0
17	49.5	0
18	52.5	0
19	55.5	0
20	58.5	0
21	61.5	0

To study the effect of the mesh simulations are performed for coarse, medium and fine three meshes, whose resolution is doubled successively. The number of nodes and the minimum and maximum mesh size in the axial and radial directions of each mesh are listed in Tab. 2.

Tab. 2 Mesh size information for mesh-independency studies

	N_{axial}	N_{radial}	$\Delta_{x,min}$ (mm)	$\Delta_{x,max}$ (mm)	$\Delta_{z,min}$ (mm)	$\Delta_{z,max}$ (mm)	y^+_{max}	CPU time (s)
coarse	250	12	3.0	13.1	16.0	36.3	1656	2.098×10^5
medium	500	24	1.5	6.3	8.0	18.0	812	2.88×10^5
fine	1000	48	0.75	2.8	4.0	9.0	401	4.619×10^5

The influence of the mesh resolution on the predictions for cross-section averaged void fraction, liquid temperature as well as radial void fraction profile is illustrated in Fig. 5(a) ~ 5(c). As one can see, the results using the three meshes coincide with each other. Only slight deviations are present at the wall peak of the radial void fraction profiles (see Fig. 5(c)). The medium mesh is used further in this work.

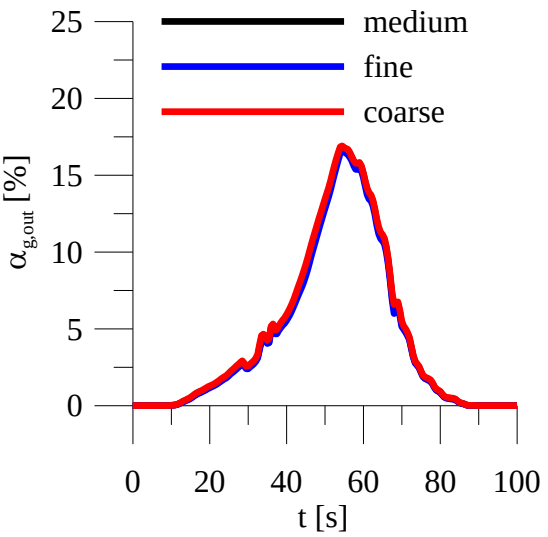

(a) cross-section averaged void fraction at WMS plane

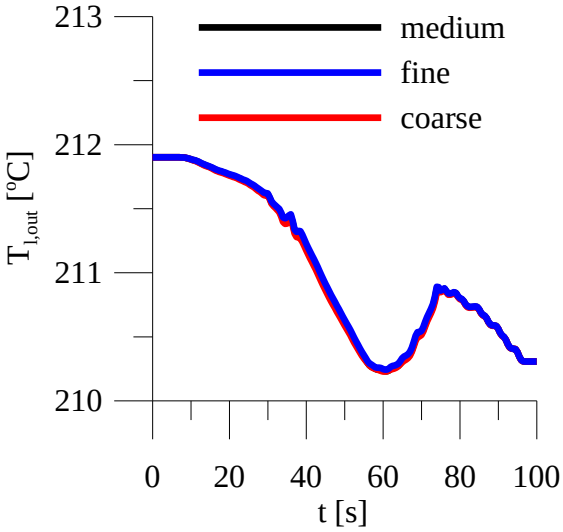

(b) liquid temperature at outlet

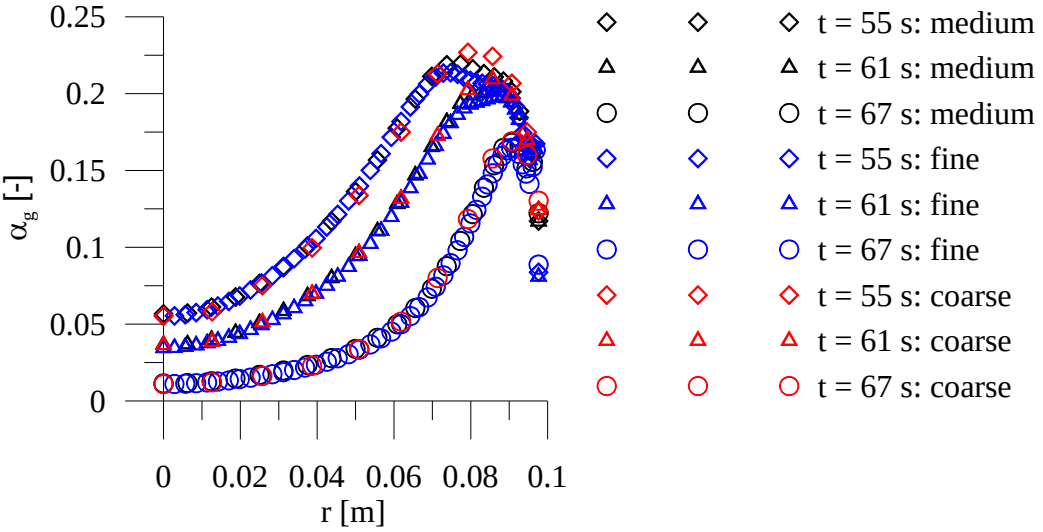

(c) radial void fraction profile

Fig. 5 The result of mesh-independency studies

5.2 Simulation results

The comparison between the simulated and the measured evolution of cross-section averaged void fraction, liquid temperature at the WMS plane, and the absolute pressure is shown in Fig. 6(a) ~ 6(c). It is evident that the start and cease of flash evaporation of water governed by the opening and closing the blow-off value is well captured by the simulation. Figure 6(a) shows that the onset of vaporization occurs slightly earlier than the experimental observation, which may be related to an over-prediction of the nucleation rate. In the investigated case wall nucleation is found to be predominant, while the contribution of bulk nucleation is negligible but it increases with the opening degree of valve as well as the pressure level. Overall, the performance of the applied nucleation model is reasonable. The predicted temporal course of water temperature at the WMS plane is in consistency with the measured one as shown in Fig. 6(b). Water becomes

superheated shortly after the blow-off valve opens (t<5 s). As the superheat degree exceeds a limit, water begins to evaporate and cool down. It reaches almost the saturation temperature before the value begins to close again. The decreasing temporal course of the water temperature is similar to that of the pressure as shown in Fig. 6(c). It is because the inlet temperature is approximately equal to the saturation temperature corresponding to the pressure level in the steam drum (see Fig. 1). In the period of valve closing (t>58 s) water temperature increases as a response to pressure recovery, and subsequently the evaporation is suppressed. A slight over-prediction of the water temperature is observed in Fig. 6(b), which is supposed to be caused by the under-prediction of the total evaporation rate (see Fig. 6(a)). Nevertheless, the maximum deviation is less than 0.5 K, and the prediction is reliable. The absolute pressure is a crucial parameter in the simulation, since it determines the saturation temperature and liquid superheat degree available for vaporization. It is calculated by

$$p = p_{ref} + \rho g\left(z_{ref} - z\right) + p_{static} \tag{23}$$

In the simulation, the reference pressure p_{ref} is set to 2.0 MPa and the reference position z_{ref} is fixed at the WMS plane. In addition, the measured relative static pressure is provided as boundary conditions for the outlet. So, if the prediction at the inlet conforms to the measurement, the absolute pressure in the whole domain is reliably predicted. As shown in Fig. 7(c) the predictions coincide with the measurements at both the inlet and outlet.

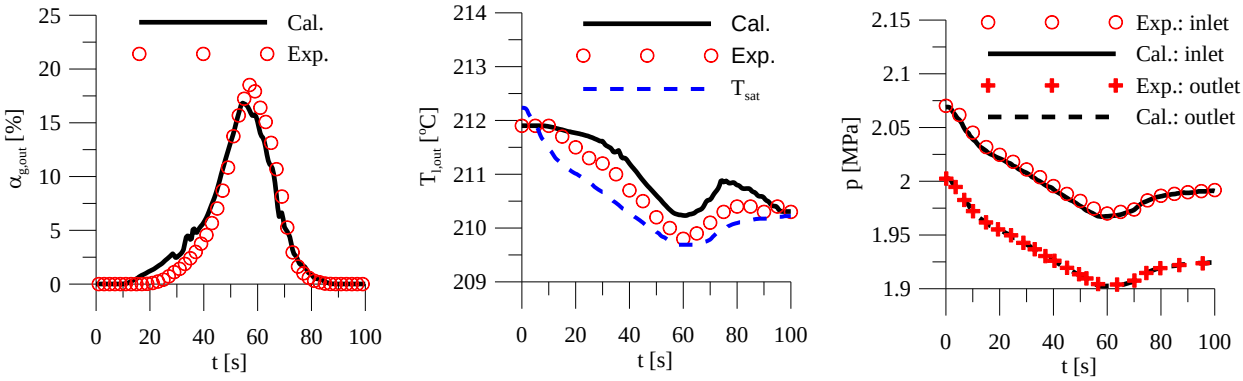

(a) (b) (c)

Fig. 6 Comparison between measured and calculated (a) outlet void fraction, (b) outlet liquid temperature, (c) absolute pressure

The spreading and returning of the evaporation wave inside the pipe along the axial and radial direction is illustrated in Fig. 7. The evaporation of water is initiated near the pipe wall (right side) at the top end of the pipe due to a low hydrostatic pressure there and the contribution of wall nucleation. Then the evaporation wave propagates downwards to the bottom of the pipe as depressurization continues. The increase of void fraction in the pipe centre results mainly from the migration of bubbles from the wall under the effect of lift force [41]. During the propagation or redistribution, the steam volume fraction increases globally. It reaches the maximum around t = 60s, when the blow-off valve begins to close again. Subsequently, the cease of vaporization and reduction of void fraction starts from the bottom and centre of the pipe. The evaporation region shrinks back to the wall, and finally the flow inside the pipe returns to single-phase water for *t>80s*.

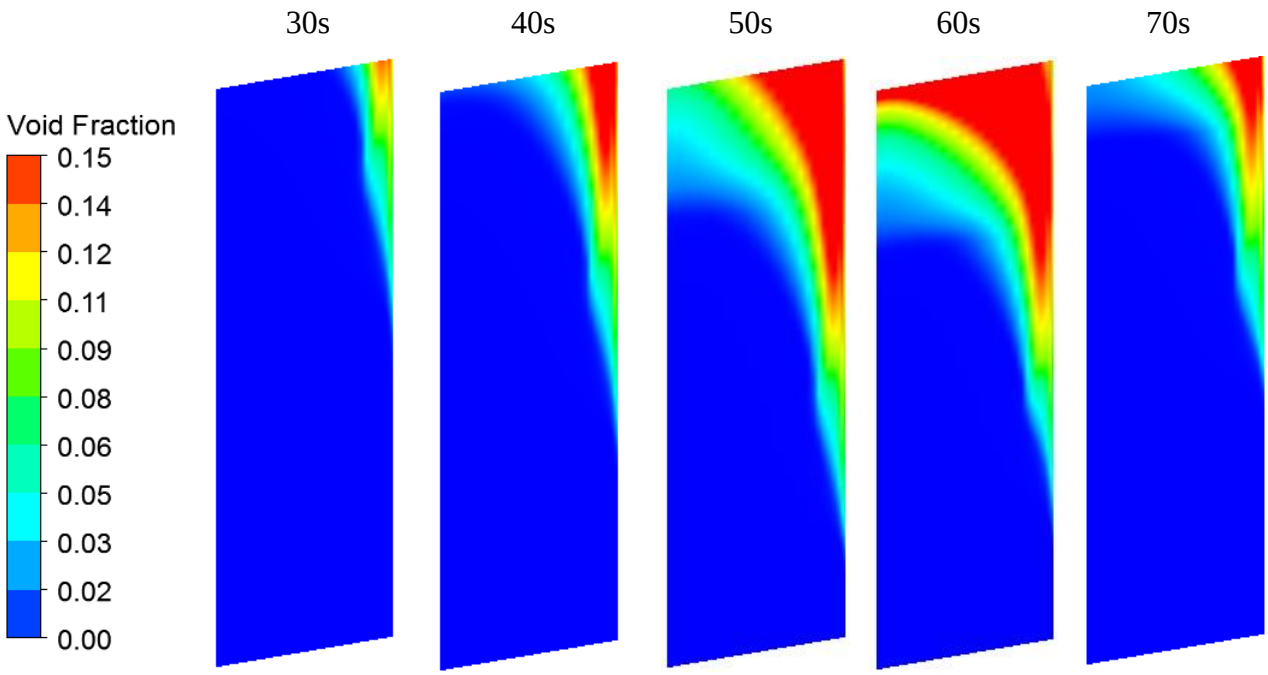

Fig. 7 Spatial formation and distribution of steam inside the pipe (left: centre, right: wall)

The evolution of cross-section averaged steam volume fraction along the pipe depth is compared with the data, which is shown in Fig. 8. It is worth mentioning that the data provided by the experiment are not measurements but calculations according to the measured pressure drop along the pipe. According to the pressure measurement positions the vertical pipe was divided into five sections, and an average gas volume fraction was calculated according to the pressure loss over the section. The void fraction at the WMS plane obtained in this way is found to be smaller than the WMS measurement. On the other hand, the simulation results are sampled from the vertical positions z=1.0 m, 2.0 m, 3.0 m, 4.0 m, 5.0 m, 6.0 m, 7.0 m and 8.0 m. Both the simulation and the experiment prove that the liquid at the inlet remains in single phase. Thus the assumption made in defining the inlet conditions for the simulation is acceptable. Although quantitative difference exists, the measured and predicted tendency of the evolution from t=20s to t=70s conform to each other.

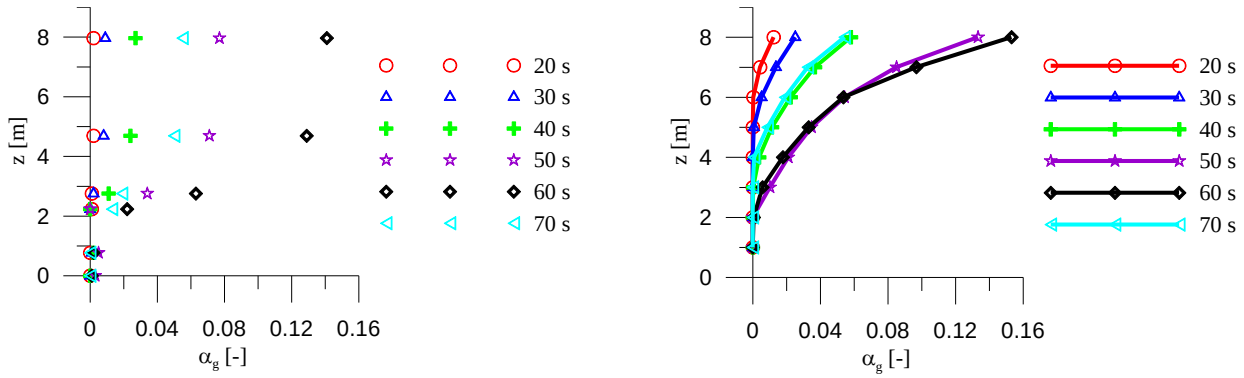

(a) experiment (b) simulation

Fig. 8 Evolution of void fraction along the pipe height

Figure 9 illustrates the evolution of radial void fraction profile with the time. The process that bubbles grow and migrate from the wall to the pipe centre for t<55s, and shrink and return to the wall after t=55s is demonstrated in both experiments and simulations. The over-prediction of the wall peak at the early stage, e.g. t=19s or 25s, indicates an over-estimation of the wall nucleation rate. Nevertheless, the measured and predicted profiles are in a pretty good agreement at t=49s, although a slight under-prediction is present at t = 55s. Further, according to the measurement bubbles are dispersed substantially over the cross-section of the pipe in the period from t=55s to t=61s, which is however not reproduced by the model. It is supposed to be related to the prediction of the lift and turbulence dispersion force, which are main factors affecting the transverse motion of bubbles.

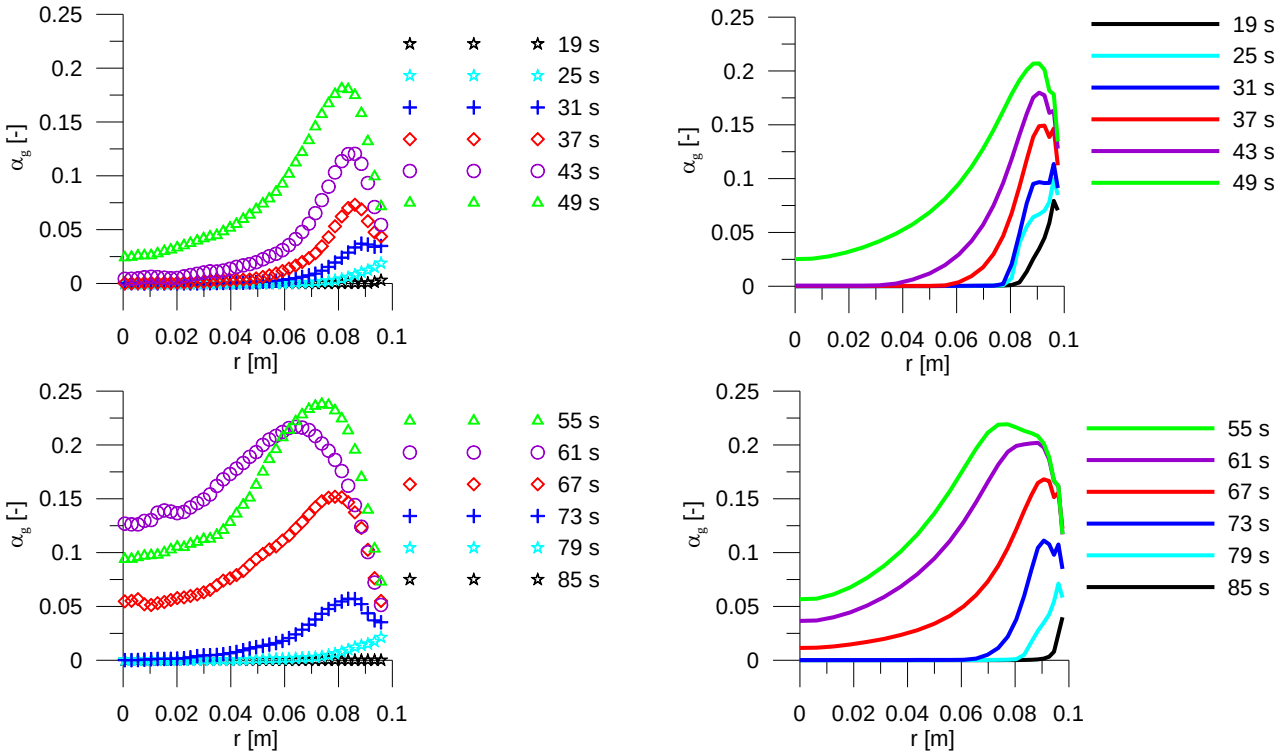

(a) experiment (b) simulation

Fig. 9 Radial profile of void fraction at the WMS plane

More details about the interphase momentum transfer are revealed by the comparison between the measured and the simulated gas velocity (vertical component) profile. As shown in Fig. 10, the acceleration and deceleration of liquid and thus gas in the near-wall region due to the generation and disappearance of bubbles are evident in both experiment (left) and simulation (right). However, the predicted variation is much more drastically than the measured one, which leads to too high wall-peaks and too low central velocities in comparison to the measurement. It indicates that further polishing of the interphase momentum transfer models, e.g. drag force, is necessary.

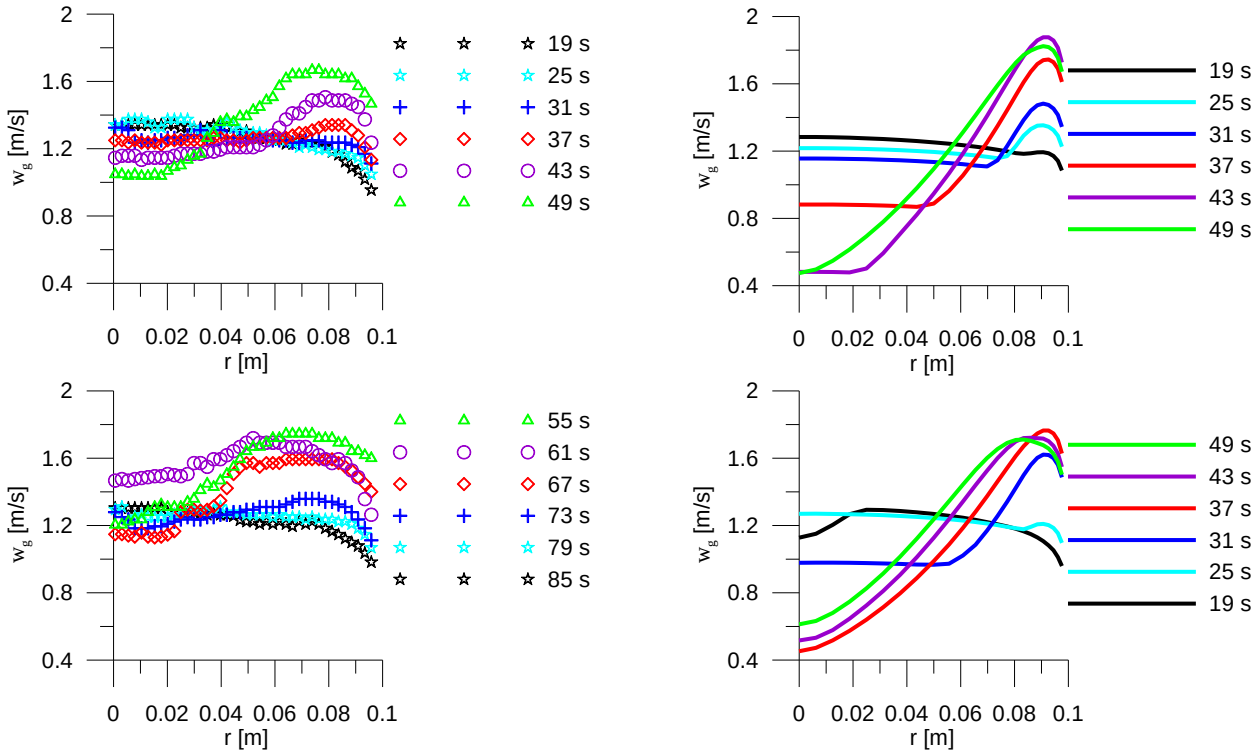

(a) experiment (b) simulation

Fig. 10 Radial profile of vertical gas velocity at the WMS plane

As shown in Fig. 11, the evolution of the bubble size distribution averaged at the WMS plane is well captured. It evidences that the applied poly-disperse approach and the closure models for bubble coalescence and growth due to phase change are reliable. During the pressure release transient, small bubbles are formed in superheated liquid as a result of nucleation and subsequently grow due to the evaporation and coalescence. The maximum size of bubbles can reach around 60 mm.

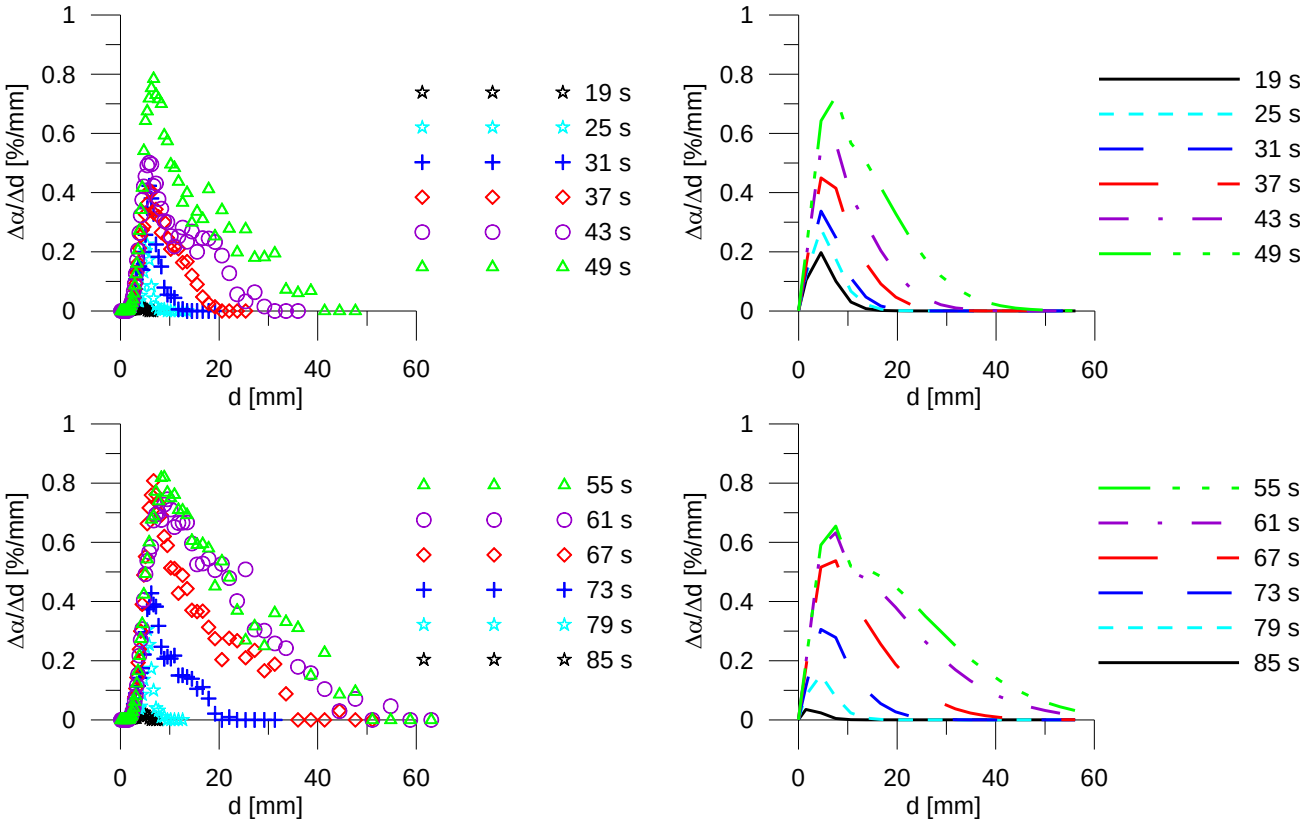

Fig. 11 Evolution of bubble size distribution at the WMS plane (left: experiment, right: simulation)

The evolution of local Sauter mean bubble diameter is shown in Fig. 11. Since it is assumed that initially all the bubbles have the smallest representative size, the mean diameter at t=0s is around 1.5 mm (see the discretization in Tab. 1). The slight variation is caused by the hydrostatic pressure change. At t=10s, bubbles begin to grow at the top of the pipe due to evaporation and coalescence. Up to t=60s, the phase change region expands, and the maximum mean bubble diameter reaches a value around 26 mm. The large bubbles are located in the pipe centre region. As the pressure is recovered due to the closing of the valve, the evaporation is suppressed after t=70s, and the mean bubble diameter decreases again. Further, it is interesting to observe that in the lower part of the pipe, where no phase change occurs, the mean bubble diameter near the pipe wall increases also as the result of coalescence.

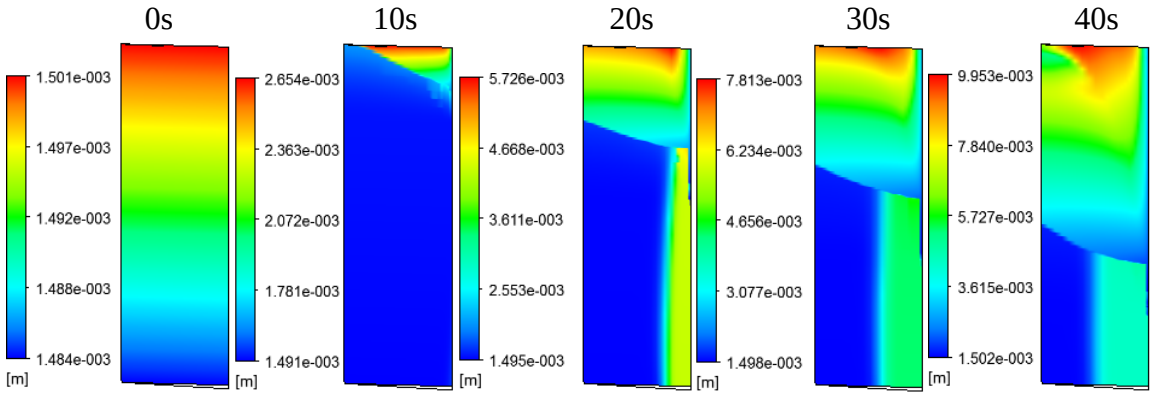

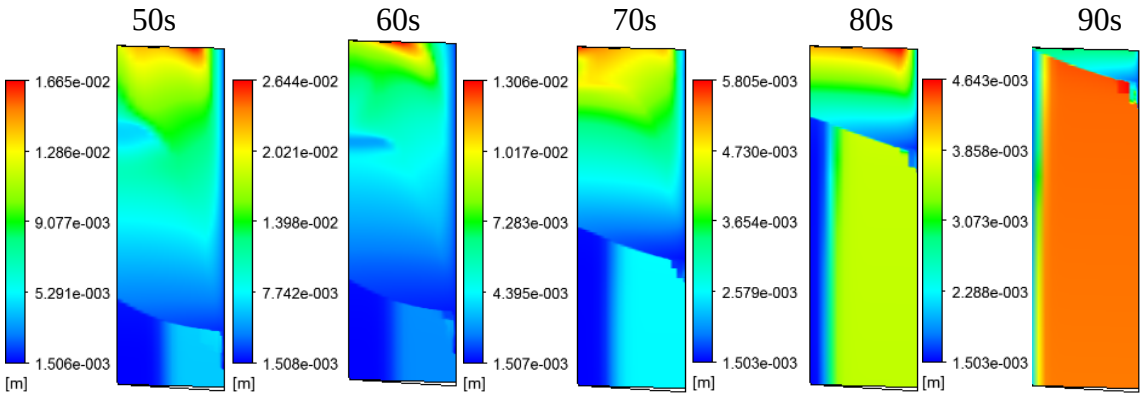

Fig. 12 Snapshot of Sauter mean bubble diameter in the domain at different time points

5 Conclusions

Flashing of liquid during depressurization is an extremely complex process accompanied with rapid interphase mass, heat and momentum transfer and bubble dynamics. So far CFD attempts in the literature are all based on the simplifying assumption of mono-dispersity of vapour bubbles, which departs far away from the physical picture of the phenomenon. For example, in the pressure release experiment that investigated in this work a broad and varying size spectrum of bubbles were detected. Despite this, poly-disperse modelling of boiling two-phase flows represents so far a challenge due to lack of data for independent validation. A poly-disperse approach is developed, which accounts for the effect of nucleation, coalescence and phase change on the evolution of local bubble size distribution. The comparison with experimental data evidences that the flash evaporation process induced by the action of the blow-off valve is reproduced well by the model. Satisfactory predictions of cross-section averaged bubble size and flow parameters such as void fraction and liquid temperature are obtained, which demonstrates the effectiveness of the poly-disperse method and the mechanistic model proposed for estimating the interphase heat transfer coefficient. In addition, the evolution of radial void fraction profile, local bubble size distributions as well as the mean bubble diameter during the flash evaporation is predicted reliably.

Acknowledgement

The authors would like to thank all members of the TOPFLOW team who contributed to the successful performance of these experiments. Special thanks to Mr. Matthias Beyer and Mr. Lutz Szalinski for helpful discussion about the experimental procedure and preparation of the data used in this work.

References

1. Mathkovič, M. and Končar, B. Bubble departure diameter prediction uncertainty. Science and Technology of Nuclear Installations, Hindawi Publishing Corporation, Volume 2012, Article ID 863190, 7 pages, doi:10.1155/2012/863190, 2012
2. Janet J. P., et al. Heterogeneous nucleation in CFD simulation of flashing flows in converging-diverging nozzles. International Journal of Multiphase Flow, 74, 106–117, 2015

3. Angielczyk, W., et al. 1-D modelling of supersonic carbon dioxide two-phase flow through ejector motive nozzle. International Regrigeration and Air Conditioning Conference, Paper 1102. http://docs.lib.purdue.edu/iracc/1102, 2010
4. Neroorkar, K.D. Modeling of flash boiling flows in injectors with Gasoline-Ethanol fuel blends. PhD thesis, University of Massachusetts – Amherst, 2011
5. Schaefer, F. Manera, A. Investigation of flashing-induced instabilities at CIRCUS test facility with the code ATHLET. International Journal of Nuclear Energy Science and Technology, 2, 209-218, 2006
6. Kozmenkov, Y., et al. Validation of the RELAP5 code for the modeling of flashing-induced instabilities under natural-circulation conditions using experimental data from the CIRCUS test facility. Nuclear Engineering and Design, 243, 168-175, 2012
7. Riznic, J. and Ishii, M. Bubble number density in vapour generation and flashing flow. International Journal of Heat and Mass Transfer, 32, 1821-1833, 1989
8. Blinkov, V.N. and Jones, O.C. Nigmatulin, B.I. Nucleation and flashing in nozzles – 2. International Journal of Multiphase Flow, 19, 965-986, 1993
9. Giese, T. and Laurien, E. A thermal based model for cavitation in saturated liquids. Zeitschrift für angewandte Mathematik und Mechanik, 2001
10. Giese, T. and Laurien, E. Experimental and numerical investigation of gravity-driven pipe flow with cavitation. Proceedings of 10th International Conference on Nuclear Engineering (ICONE10), Arlington, Virginia, USA, April 14-18, 2002
11. Laurien, E. and Giese, T. Exploration of the two fluid model of two-phase flow towards boiling, cavitation and stratification. The 3rd International Conference on Computational Heat and Mass Transfer, Banff, Canada, May 26 -30, 2003
12. Laurien, E. Influence of the model bubble diameter on three-dimensional numerical simulations of thermal cavitation in pipe elbows, 3rd International Symposium on Two-Phase Flow Modelling and Experimentation, Pisa, 22-24 September 2004
13. Frank, Th. Simulation of flashing and steam condensation in subcooled liquid using ANSYS CFX, 5th Joint FZR & ANSYS Workshop "Multiphase Flows: Simulation, Experiment and Application", Dresden, Germany, April 26-27, 2007.
14. Maksic, S. and Mewes, D. CFD-Calculation of the flashing flow in pipes and nozzles. Proc. ASME FEDSM'02, Montreal, Quebec, Canada, 14-18 July, 2002
15. Marsh, C.A. and O'Mahony, A.P. Three-dimensional modelling of industrial flashing flows. Progress in Computational Fluid Dynamics, 9, 393-398, 2009
16. Mimouni, S., et al. Modelling and computation of cavitation and boiling bubbly flows with the NEPTUNE_CFD code. Nuclear Engineering and Design, 238, 680-692, 2008
17. Liao, Y. and Lucas, D. Computational modelling of flash boiling flows: A literature survey. International Journal of Heat and Mass Transfer, 111, 246-265, 2017
18. Edwards, A. R. and O'Brien, T.P. Studies of phenomena connected with the depressurization of water reactors. British Nuclear Energy Society, 9, 125-135, 1970
19. Liao, Y. et al. Assessment of CFD predictive capacity for flash boiling. CFD4NRS-5, Sept. 09 -11, Zurich, Switzerland, 2014
20. Liao, Y., et al. Flashing evaporation under different pressure levels. Nuclear Engineering and Design, 265, 801-813, 2013

21. Liao, Y. and Lucas, D. 3D CFD simulation of flashing flows in a converging-diverging nozzle. Nuclear Engineering and Design, 292, 149-163, 2015
22. Liao, Y., et al. CFD modeling of flashing instability in natural circulation cooling systems. Proceedings of the 26th International Conference on Nuclear Engineering, ICONE26, July 23-26, 2018, Hammersmith, London, England, 2018
23. Wallis, G.B. Critical two-phase flow. International Journal of Multiphase Flow, 6, 97-112, 1980
24. Liao, Y. and Lucas, D. Evaluation of interfacial heat transfer models for flashing flow with two-fluid CFD. Fluids 2018, 3, 38; doi:10.3390/fluids3020038, 2018
25. Shin, T.S. and Jones, O.C. Nucleation and flashing in nozzles-1: A distributed nucleation model. International Journal of Multiphase Flow, 19, 943-964, 1993
26. Blander, M. and Katz, J. L. Bubble nucleation in liquids. AIChE Journal, 21, 833-848, 1975
27. Ansys, C. Release 14.5, ANSYS CFX-solver theory guide, 2012
28. Liao, Y. and Lucas, D. Possibilities and limitations of CFD simulation for flashing flow scenarios in nuclear application. Energies 2017, 10, 139; doi:10.3390/en10010139, 2017
29. Lucas, D., et al. Experiments on evaporating pipe flow. The 14th International Topical meeting on Nuclear Reactor Thermalhydraulics, NURETH-14, Toronto, Ontario, Canada, September 25-30, 2011
30. Schaffrath, A., et al. TOPFLOW—A new multipurpose thermalhydraulic test facility for the investigation of steady state and transient two-phase flow phenomena. Kerntechnik, 66, 209-212, 2001
31. Liao, Y. et al. Baseline closure model for dispersed bubbly flow: bubble coalescence and breakup. Chemical Engineering Science, 122, 336-349, 2015
32. Lucas, D., et al. A strategy for the qualification of multi-fluid approaches for nuclear reactor safety. Nuclear Engineering and Design, 299, 2–11, 2016
33. Liao, Y., et al. Eulerian modelling of turbulent bubbly flow based on a baseline closure concept. Nuclear Engineering and Design, 337, 450–459, 2018
34. Ranz, W.E., Marshall, W.R. Evaporation from drops. Chemical Engineering Progress, 48, Part I: 141-146, Part II: 173-180, 1952
35. Liao, Y., et al. A baseline closure concept for simulating bubbly flow with phase change: Interfacial heat transfer coefficient. CFD4NRS-7 OECD-NEA & IAEA Workshop, September 4-6, 2018, Shanghai, China, 2018
36. Krepper, E., et al. A population balance approach considering heat and mass transfer-Experiments and CFD simulations. Nuclear Engineering and Design, 241, 2889-2897, 2011
37. Lucas, D., et al. Extension of the inhomogeneous MUSIG model for bubble condensation. Nuclear Engineering and Design, 241, 4359-4367, 2011
38. Liao, Y., et al. A discrete population balance equation for binary breakage. International Journal of Numerical Methods in Fluids, 2018;1–14; DOI: 10.1002/fld.4491, 2018
39. Liao, Y. and Lucas, D. Poly-disperse simulation of condensing steam-water flow inside a large vertical pipe. International Journal of Thermal Sciences, 104, 194-207, 2016
40. Rohatgi, U. and Reshotko, E. Non-equilibrium one-dimensional two-phase flow in variable area channels. In: Non-Equilibrium Two-Phase Flows; Proceedings of the Winter Annual

Meeting, Houston, Tex., November 30–December 5, 1975, Meeting Sponsored by the American Society of Mechanical Engineers, New York, vol. 1. American Society of Mechanical Engineers, 47–54, 1975

41. Tomiyama, A. Struggle with computational bubble dynamics. ICMF'98, 3rd International Conference of multiphase Flow, Lyon, France, June 8-12, 1998